ACS APPLIED ELECTRONIC MATERIALS

pubs.acs.org/acsaelm Article

Effect of Electron Doping on the Crystal Structure and Physical Properties of an $n = 3$ Ruddlesden–Popper Compound $La_4Ni_3O_{10}$

Manimuthu Periyasamy,* Lokanath Patra, Øystein S. Fjellvåg, Ponniah Ravindran, Magnus H. Sørby, Susmit Kumar, Anja O. Sjåstad, and Helmer Fjellvåg*

Cite This: *ACS Appl. Electron. Mater.* 2021, 3, 2671–2684 Read Online

ACCESS | Metrics & More | Article Recommendations | Supporting Information

ABSTRACT: The physical properties of $La_4Ni_3O_{10}$ with a two-dimensional (2D)-like Ruddlesden–Popper-type crystal structure are extraordinarily dependent on temperature and chemical substitution. By introducing Al^{3+} atoms randomly at Ni sites, the average oxidation state for the two nonequivalent Ni cations is tuned and adopts values below the average of +2.67 in $La_4Ni_3O_{10}$. $La_4Ni_{3-x}Al_xO_{10}$ is a solid solution for $0.00 \leq x \leq 1.00$ and is prepared by the citric acid method, with attention paid to compositional control and homogeneity at low Al level (x) concentrations. The samples adopt a slightly distorted monoclinic structure [$P2_1/a$ ($Z = 4$)], evidenced by peak broadening of the (117) reflection. We report a remarkable effect on the electronic properties induced by tiny amounts of homogeneously distributed Al cations, with clear correspondence between resistivity, magnetization, diffraction, and density functional theory (DFT) data. DFT shows that electronically, there is no significant difference between the nonequivalent Ni atoms and no tendency toward any Ni^{3+}/Ni^{2+} charge ordering. The resistivity changes from metallic to semiconducting/insulating with increasing band gap at higher Al levels, consistent with results from DFT. The metal-to-metal (M-T-M) transition reported for $La_4Ni_3O_{10}$, which is often interpreted as a charge density wave, is maintained until $x = 0.15$ Al level. However, the temperature characteristics of the resistivity change already at very low Al levels ($x \leq 0.03$). A coupling of the M-T-M transition to the lattice is evidenced by an anomaly in the unit cell dimensions. Moreover, there is an excellent correlation between the resistivity and magnetization data shown by the metallic and Pauli paramagnetic regime for $La_4Ni_{3-x}Al_xO_{10}$ with $x < 0.25$. The introduction of the fixed +3 oxidation state of Al atoms randomly at the Ni sites reduces the overall oxidation state of $Ni^{2.67+}$ by keeping the oxygen stoichiometry unchanged. In addition, the nonmagnetic Al^{3+} for Ni is likely to block Ni–O–Ni exchange pathways through –Ni–O–Al–O–Ni– fragments into the network of corner-shared octahedra with the emergence of possible short-range ferromagnetic ordering of the ferromagnetic domains/clusters that are formed due to Al substitutional disorder in a paramagnetic insulating matrix.

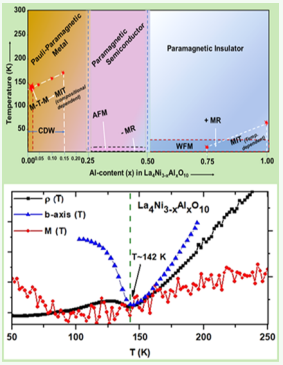

KEYWORDS: *Ruddlesden–Popper, nickelates, quasi-2D, Pauli paramagnetic, charge density waves, density functional theory*

1. INTRODUCTION

The Ruddlesden–Popper (RP) series of nickelates $La_{n+1}Ni_nO_{3n+1}$ attract interest owing to their layer-like character, features resembling high-T_c superconductors, and their physical properties.[1−4] The RPn crystal structure consists of n consecutive perovskite layers, $(LaNiO_3)_n$, alternating with rock-salt-like layers of LaO, *i.e.*, $(LaO)(LaNiO_3)_n$.[5] The presence of half a rock-salt-like layer influences the physical properties, and the number of the perovskite blocks (n) plays an important role due to their two-dimensional (2D)-like features.[6−8] With increasing n, the electrical behavior changes from insulating to metallic.[9,10] Their structures are closely related, though, with different symmetries, where La_2NiO_4 is tetragonal,[11] $La_3Ni_2O_7$ is orthorhombic,[12] and $La_4Ni_3O_{10}$ is slightly monoclinically distorted (pseudo-orthorhombic)[2,4,13] at room temperature. Oxygen nonstoichiometry (surplus) is quite extensive for the $n = 1$ member with additional O atoms confined in the rock-salt-like layers.[14]

Earlier, we reported on crystal structure and phase transitions for $La_4Co_3O_{10}$ and $La_4Ni_3O_{10}$ and their solid solutions.[13,15−18] In high-resolution synchrotron powder diffraction patterns, the monoclinic distortion is manifested by peak broadening, and in some cases, peak splitting. The $P2_1/a$ structure for $La_4Ni_3O_{10}$ was recently evaluated by density functional theory (DFT) and found to be close in energy to variants with symmetries described in space groups *Bmab*, *Pcab* as well in a smaller volume $P2_1/a$ structure ($P2_1/a$-II),[2,19,20] likewise supported by single-crystal diffraction studies.[21] Puggioni and Rondinelli found that the larger $Z = 4$ $P2_1/a$ structure transformed to the $Z = 2$ $P2_1/a$-II structure on coordinate relaxation.[2] In all cases, the differences in terms of atomic displacements are small. We note that the *Bmab* orthorhombic model well approximates the atomic arrange-

Received: March 21, 2021
Accepted: May 11, 2021
Published: May 22, 2021

ment of $La_4Ni_3O_{10}$. Pristine $La_4Ni_3O_{10}$ is a Pauli paramagnetic metal. An anomaly in the resistivity at ≈140 K is discussed in terms of a metal-to-metal (M-T-M) transition and/or charge density waves (CDW).[2,9,19,22] Further, recent experimental studies of the Fermi surface of $La_4Ni_3O_{10}$ using angle-resolved photoemission spectroscopy (ARPES) revealed a pseudo-gap at 120−150 K.[23]

The average Ni oxidation state increases for larger n values in $La_2(Ni^{2+})_1O_4$, $La_3(Ni^{2+})_1(Ni^{3+})_1O_7$, and $La_4(Ni^{2+})_1(Ni^{3+})_2O_{10}$. Further oxidation may occur by intercalated O anions in the rock-salt layers, whereas reduction gives random or ordered O vacancies and may result in an unusually low average oxidation state (+1.33 in $La_4Ni_3O_8$).[24,25] For these RPn compounds, the physical properties are closely linked to their layer-like structure and dimensionality effects.[26−29] A large number of phenomena may occur at low temperatures, like electronic and magnetic transitions, colossal magnetoresistance, and long-range magnetic order.[30−32] To expand our insights, we currently explore the effect of substitution of nonmagnetic Al^{3+} into the Ni sublattices of $La_4Ni_3O_{10}$. In general, the incorporation of chemical substitutions into $La_4Ni_3O_{10}$ is challenging, whether being substituted at the lanthanum sites with alkaline-earth cations or the Ni sites by transition-metal cations such as Mn, Co, and Cu.[13,33−35] Correspondingly, attention must be paid to avoid partial phase decomposition.

Importantly, the fixed +3 oxidation state of the Al-substituent will provide electron doping that reduces the average oxidation state of nickel in $La_4Ni_3O_{10}$ while keeping the O stoichiometry unchanged. Hence, the Al substitution will affect the average valence of Ni sites and thus the exchange interactions. This makes $La_4Ni_{3-x}Al_xO_{10}$ a very exciting system to study in detail. To minimize any potential effect of oxygen nonstoichiometry on the measured properties, all samples were heat-treated at T, pO_2 conditions recognized to give stoichiometric $La_4Ni_{3-x}Al_xO_{10}$, which also ought to secure completely filled O sites for the lower-valent Ni compositions resulting from Al substitution.

We address several open questions: (i) will Al substitution trigger a metal-to-insulator (MIT) transition as a function of temperature and/or composition? (ii) will the CDW transition of $La_4Ni_3O_{10}$ disappear or change character? (iii) will the Pauli paramagnetism transform into Curie−Weiss-like paramagnetism with localized moments and long-range magnetic order emerging at low temperatures? (iv) will we observe positive or negative magnetoresistance and how does this correlate with Al content and electrical resistivity? (v) will a change in the formal Ni^{3+}/Ni^{2+} ratio give rise to ferromagnetic-like interactions *via* a double-exchange mechanism?

Herein, we provide extensive new insights into structural, transport, magnetic, and magnetoresistance (MR) properties of $La_4Ni_{3-x}Al_xO_{10}$ ($0.00 \le x \le 1.00$) as studied by powder X-ray diffraction (PXRD), synchrotron PXRD, powder neutron diffraction (PND), magnetization, and resistivity studies. The atomic arrangement is described in space group $P2_1/a$ ($Z = 4$), partly approximated in *Bmab*. The experimental data are supported by first-principles DFT modeling with focus on electronic structure, bonding, oxidation states, magnetism, and stability.

2. METHODS

2.1. Experimental Methods. Samples of $La_4Ni_{3-x}Al_xO_{10}$ (x = 0.00−1.00) were synthesized according to the citric acid method.[13,15−18] The starting reactants were La_2O_3 (99.99%, Molycorp), $Ni(CH_3COO)_2{\cdot}4H_2O$ (≥99%, Sigma-Aldrich), $Al(NO_2)_3{\cdot}9H_2O$ (98%, Sigma-Aldrich), $C_3H_4(OH)(COOH)_3{\cdot}H_2O$ (98%, Sigma-Aldrich), and HNO_3 (min. 65%, AnalaR NORMAPUR, VWR). Prior to use, La_2O_3 was heated at 1273 K in air for 12 h and cooled to room temperature in a desiccator. The exact formula weights of the Ni and Al salts were determined gravimetrically, and standard salt solutions with accurate molar concentrations were prepared. La_2O_3 was dissolved in 6 M HNO_3 at 373 K under constant stirring before being mixed with the standard Ni and Al solutions, according to the targeted stoichiometry. Subsequently, citric acid monohydrate was added in excess during stirring and heating of the entire solution. Nitrous gas species and water were boiled off until a syrup-like solution was formed, which was dried at 453 K overnight. The obtained crust was calcined at 673 K for 4 h and 1073 K for 1 h in static air, to remove organic matter. The resulting powders were ground, pelletized, and sintered in an alumina boat at high temperatures in air for 2 days before being cooled to room temperature in a furnace. The chosen sintering temperature depended on the Al^{3+} content. For higher Al^{3+} contents, the temperature required to stabilize a phase-pure product increased. For $x = 0.00$, the sintering temperature was 1273 K, while it was 1473 K for $x = 1.00$. Further, repeated sintering after one intermediate crushing was done to enhance sample homogeneity. An overview of all nominal compositions prepared is given in Table S1 in the Supporting Information.

The oxygen content of the prepared samples was determined by cerimetric titrations and thermogravimetric analysis (TGA). Cerimetric titration was performed by dissolving Mohr salt, $(NH_4)_2Fe(SO_4)_2{\cdot}6H_2O$ (99%, Sigma-Aldrich), and a few milligrams of the sample in 1 M HCl in inert atmosphere of Ar (5 N Aga). The solution was then titrated with 0.1 M $Ce(SO_4)_2$ (volumetric, Fluka) under an inert atmosphere of flowing Ar. The exact formula weight of the Mohr salt was determined gravimetrically using three parallel measurements. The exact concentration of the $Ce(SO_4)_2$ solution was determined separately by titrating with Mohr salt. TGA was performed in N_2 (5 N Aga), O_2 (5 N Aga), and O_2/N_2 atmospheres with a Netzsch STA 449 F1 Jupiter. Heating and cooling cycles were set at 10 °C/min. Background corrections were measured with empty sample holders under the same experimental conditions to eliminate any effects from the holders and the atmosphere.

Phase content and unit cell dimensions were analyzed by means of PXRD data collected at room temperature on a Bruker D8 Discover with a Lynxeye detector and Cu Kα_1 radiation [λ = 1.5406 Å, Ge(111) Johansson monochromator]. The PXRD data collected between 20 and 100° in steps of 0.02° were analyzed by Rietveld refinements using the TOPAS V5 software.[36] The background was modeled using a Chebyshev polynomial function and a double Voigt function to fit peak shapes. The initial structural parameters were taken from previously reported data (*Bmab*, *Pcab*, monoclinic-I $P21/a$, and monoclinic-II $P21/a$) for $La_4Ni_3O_{10}$.[2,9,13,20] Overall isotropic temperature factors for each element were refined. The occupation factors were fixed based on nominal sample stoichiometry, assuming that Al cations are randomly distributed over the Ni sites. All oxygen sites were fully occupied, *i.e.*, having a fully stoichiometric RP3 phase. Absorption correction was included in the refinement.

PND data were collected at 12 K (Displex cryostat) for $La_4Ni_{2.50}Al_{0.50}O_{10}$ and $La_4Ni_2AlO_{10}$ with a high-resolution two-axis powder diffractometer PUS at the JEEP II reactor, Kjeller, Norway, using monochromatic neutrons with λ = 1.5558 Å.[37] The data were rebinned into steps of $\Delta 2\theta = 0.05°$ for the range 2θ = 10−130°. The FULLPROF suite of programs[38] was used for Rietveld refinements, evaluating different proposed modifications of $La_4Ni_3O_{10}$. The following parameters were used: linear background corrections based on 20 background points (between 10 and 130°); the pseudo-Voigt profile function; overall isotropic temperature factors for La, Ni, Al, and O were refined; and scattering lengths of 0.824, 1.03, 0.345, and 0.580 fm for La, Ni, Al, and O were taken from the program library.

https://doi.org/10.1021/acsaelm.1c00270
ACS Appl. Electron. Mater. 2021, 3, 2671−2684

Low-temperature synchrotron PXRD data were measured at BM01 (Swiss-Norwegian Beamlines, SNBL), ESRF, Grenoble, France, at a wavelength of λ = 0.71490 Å and using a 2D PILATUS2M detector.[39] Carefully ground powder was filled into a 0.3 mm diameter borosilicate capillary and cooled in an Oxford Cryostream 700+ nitrogen blower. XRD patterns were collected between 100 and 300 K at a detector distance of 300 mm. The 2D images were integrated using the SNBL Bubble software, with rebinned one-dimensional (1D) diffraction data for $0 < 2\theta < 34.8°$ and step size 0.01°.[39] The patterns were simultaneously refined in a surface refinement using the TOPAS V5 software,[36] with unit cell parameters being refined for each scan. The Stephens model for anisotropic peak broadening was refined to all scans simultaneously.[40]

A quantum design physical property measurement system (QD-PPMS) was used for property characterization. Electrical resistivity was measured on bar-shaped bulk pellets (the densities of the samples were ~84 to 86%), using in-line four-point probe contact geometry and a dc current ranging from 1 to 2 mA, for temperatures between 4 and 300 K. Magnetic properties were measured for samples held in gelatin capsules during warming cycles at both zero-field-cooled (ZFC) and field-cooled (FC) conditions over the temperature range of 4−300 K. A persistent applied magnetic field of 0.2 T was used during ZFC/FC measurements. Magnetization was measured at 4 K between fields of ±9 T. Magnetoresistance curves were measured for fields up to 9 T at 4 K.

2.2. Computational Methods. Structural optimizations were performed using the Vienna Ab initio Simulation Package (VASP).[41] We used a 7 × 7 × 3 Monkhorst−Pack k-point mesh[42] and a plane wave cutoff energy of 700 eV. Atoms were relaxed until the force on each atom was <0.1 meV/Å. The Perdew−Burke−Ernzerhof (PBE) generalized gradient approximation (GGA) functional[43] was used. Owing to earlier experience with VASP being unable to successfully determine the ground-state magnetic ordering for RP nickelates,[25] the electronic and magnetic properties of $La_4Ni_{3-x}Al_xO_{10}$ (x = 0.25, 0.50, 1.00) were studied by the full-potential linearized augmented plane wave (FP-LAPW) method as implemented in the WIEN2k code.[44] The standard GGA exchange−correlation potential within the PBE scheme was used. To describe the 3d electron−electron repulsion of the nickel cations, the GGA + U method was used in the fully localized limit (FLL). $U_{eff} = U - J$ (where U and J are on-site Coulomb repulsion and exchange interaction, respectively) was used, with U_{eff} = 6 eV. The muffin-tin radii for La, Ni, Al, and O were chosen to be 2.38, 1.91, 1.77, and 1.62 au, respectively. Integrations in reciprocal space were performed using 108 spatial k-points in the irreducible wedge of the Brillouin zone.

3. RESULTS

3.1. Crystal Structure. We initiated our investigations on the $La_4Ni_{3-x}Al_xO_{10}$ (x = 0.00−1.00) system by considering the crystal structure of the samples. All $La_4Ni_{3-x}Al_xO_{10}$ samples were synthesized according to the citric acid method, with special attention to the low-Al-content samples to assure good homogeneity concerning the Al/Ni distribution. Characterization by PXRD showed phase-pure RP3 samples for $0.00 \leq x \leq 1.00$. Possible oxygen nonstoichiometry in $La_4Ni_3O_{10}$ has been discussed by several authors; however, in line with our earlier studies,[13,15,18] we could not prove any significant departure in oxygen content from the ideal stoichiometry. The measured oxygen nonstoichiometries in $La_4Ni_{3-x}Al_xO_{10}$ samples were comparable to the experimental errors (standard deviations of TGA < 1% and cerimetric titration ±0.02). Therefore, the oxygen content is considered as 10.00 for all synthesized samples (x = 0.00−1.00). These findings suggested that the samples are stoichiometric and that the samples are well suited for electron doping studies of $La_4Ni_3O_{10}$.

The unit cell dimension of $La_4Ni_{3-x}Al_xO_{10}$ (x = 0.00−1.00) changes smoothly with increasing Al content according to Rietveld refinements with an overall volume contraction (Figure 1). This is consistent with the smaller ionic radius of

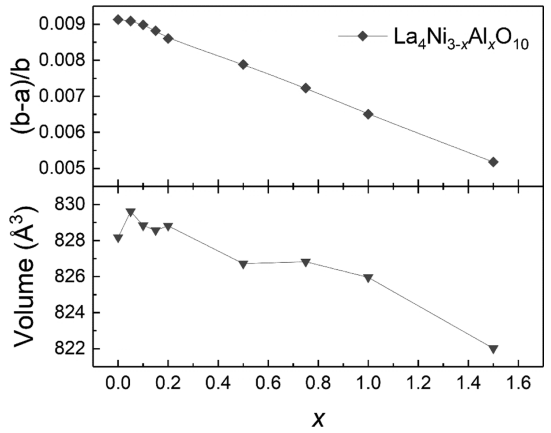

Figure 1. Unit cell volume (bottom) and degree of unit cell distortion in terms of $|(b - a)/a|$ (top) versus Al substitution (x) for $La_4Ni_{3-x}Al_xO_{10}$ from Rietveld refinements in space group *Bmab*.

Al^{3+} (0.535 Å) compared to Ni^{3+} (0.56 Å) and Ni^{2+} (0.69 Å).[45] The degree of distortion in the *ab* plane diminishes for higher Al levels (Figure 1, top). As discussed above, Al substitution provides electron doping to the Ni atoms. The Ni-average oxidation state is thereby lowered from +2.67 for x = 0.00 to +2.60 for x = 0.50 and +2.50 for x = 1.00.

The crystal structure of $La_4Ni_{3-x}Al_xO_{10}$ is revisited based on the recent DFT study that suggests a smaller monoclinic unit cell for the ground state.[2] To clarify which of the four theoretically reported structures in refs 2, 9, 13, 19 comply with our samples, we evaluated home lab PXRD, synchrotron PXRD, as well as PND data. In the case of lower-quality/lower-resolution data (home lab; neutron), the differences in fits are small for these four structures. The departure from the orthorhombic metric is tiny with $\beta < 90.2°$ for a description in space group $P2_1/a$. Such minor monoclinic distortion was earlier identified by peak broadening in high-resolution powder synchrotron diffraction patterns of $La_4Co_3O_{10}$ and $La_4Ni_{3-x}Co_xO_{10}$ solid solution.[13,15,16] Hence, the peak width of (117) is a good measure of the degree of monoclinic distortion. This was currently evaluated by comparing the peak profiles of $(117/11\bar{7})$, (200), and (020) for $La_4Ni_{3-x}Al_xO_{10}$ (see Figure 2), and it is evident that (117) peak has a broader profile than the (200) and (020) reflections; hence, $La_4Ni_{3-x}Al_xO_{10}$ exhibits a monoclinic distortion. A sketch of the crystal structure is shown in Figure S1 in the Supporting Information.

To further evaluate our conclusion from diffraction data, we turned to DFT and optimized the experimental descriptions of the orthorhombic and monoclinic variants of $La_4Ni_3O_{10}$. The total energy versus volume curves for the $P21/a$ and *Bmab* models are shown in Figure 3. Our calculations show that the monoclinic structure is more stable, however with a small energy difference (34 meV/f.u.). Therefore, DFT calculations support our conclusion from the analysis of diffraction data, *i.e.*, that $La_4Ni_3O_{10}$ adopts the monoclinic structure ($P2_1/a$). By approximating the structure in space group *Bmab*, the number of coordinate variables is reduced from 48 to 13, allowing us to use home laboratory data to derive variations in volume and atomic coordinates. Intensity profiles from the Rietveld fits are shown in Figure S2 in the Supporting

https://doi.org/10.1021/acsaelm.1c00270
ACS Appl. Electron. Mater. 2021, 3, 2671−2684

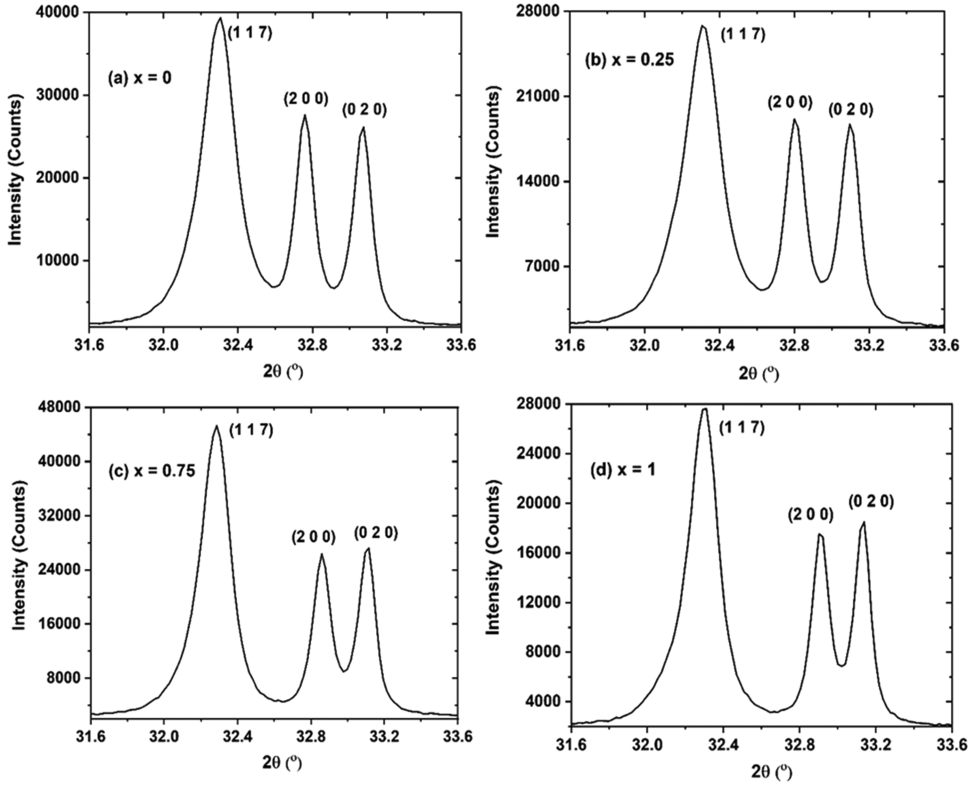

Figure 2. (a) Home laboratory powder X-ray diffraction data (left; λ = 1.5406 Å) showing a selected 2θ range where the enhanced peak width of (117)/(11$\bar{7}$) is evident compared to (020) and (200); space group *P*21/*a*. (b–d) The (117) peak broadening is also evident for Al substituted samples.

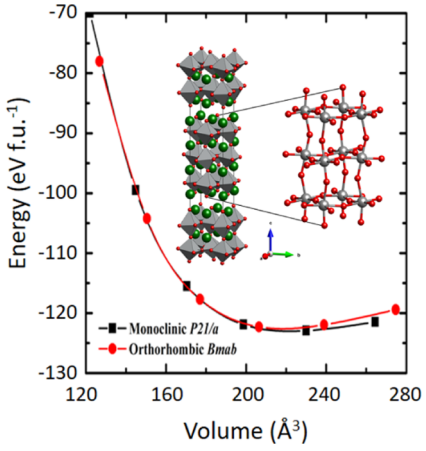

Figure 3. Total energy versus volume (per f.u.) curves for *Bmab* and *P*21/*a* structures of $La_4Ni_3O_{10}$, which show that the *P*21/*a* structure indeed is most stable. The inset shows $La_4Ni_3O_{10}$ in the stable *P*21/*a* structure. Green, gray, and red atoms correspond to lanthanum, nickel, and oxygen.

Information. When exploring the two possible models, we note that the derived unit cell dimensions are very similar, with $La_4Ni_3O_{10}$ (*Bmab*) a = 5.4167(8) Å, b = 5.4667(5) Å, and c = 27.967(4) Å, whereas for monoclinic (*P*21/*a*), a = 5.4166(4) Å, b = 5.4667(3) Å, and c = 27.980(2) Å (and β = 90.18°).

The Rietveld fit to the PND data for $La_4Ni_{2.50}Al_{0.50}O_{10}$ at 12 K is given in Figure 4. The diffraction patterns of $La_4Ni_{2.50}Al_{0.50}O_{10}$ and $La_4Ni_2AlO_{10}$ are well described by their nuclear structure; hence, long-range magnetic ordering is absent. The crystal structure contains two different types of Ni environments, one located at the center of the perovskite block (Ni2) and the other at the outer part of the perovskite block (Ni1) (see Figure S1 in the Supporting Information). Based on the difference in scattering lengths between the Ni and Al atoms, we evaluated whether any preferences existed for Al substitution to either of the two Ni sites. No such preference was detected. Hence, we conclude that Ni and Al are randomly distributed on the octahedral sites. For clarity, note that both *Bmab* and *P*21/*a* have two nonequivalent Ni sites. However, due to symmetry, the *Bmab* structure has 1 × Ni1 and 1 × Ni2 sites, whereas *P*21/*a* has 2 × Ni1 and 2 × Ni2 sites. The Ni oxidation (charge) state and the Ni–O bonding for the nonequivalent Ni cations are evaluated using the orbital-projected DOS and Born effective charge (BEC). In an ideal octahedral crystal field, the d-orbitals split into triply degenerate t_{2g} and doubly degenerate e_g states. In monoclinic fields, these degeneracies are lifted. However, in $La_4Ni_3O_{10}$, these levels are broadened into overlapping bands, and metallicity appears.

The charge difference between the Ni1 and Ni2 muffin tin spheres for $La_4Ni_2AlO_{10}$ is about 0.06e, which is minute compared to a possible nominal charge (ionicity) difference of 1e in the case of charge ordering of Ni1 and Ni2. Figure 5 shows the orbital-projected DOS for Ni1 and Ni2 in a theoretical ferromagnetic ground state. For the Ni1 and Ni2 sites, both the majority and minority spins of the d_{xy} and d_{xz} orbitals are fully occupied. Similarly, the minority spin states of e_g states are almost empty. The d_{xy} orbitals for both types of Ni ions possess partial occupancy in the minority spin channel, whereas the majority channel is fully occupied. The integrated DOS gives 0.7e and 0.6e for Ni1 and Ni2, respectively.

https://doi.org/10.1021/acsaelm.1c00270
ACS Appl. Electron. Mater. 2021, 3, 2671–2684

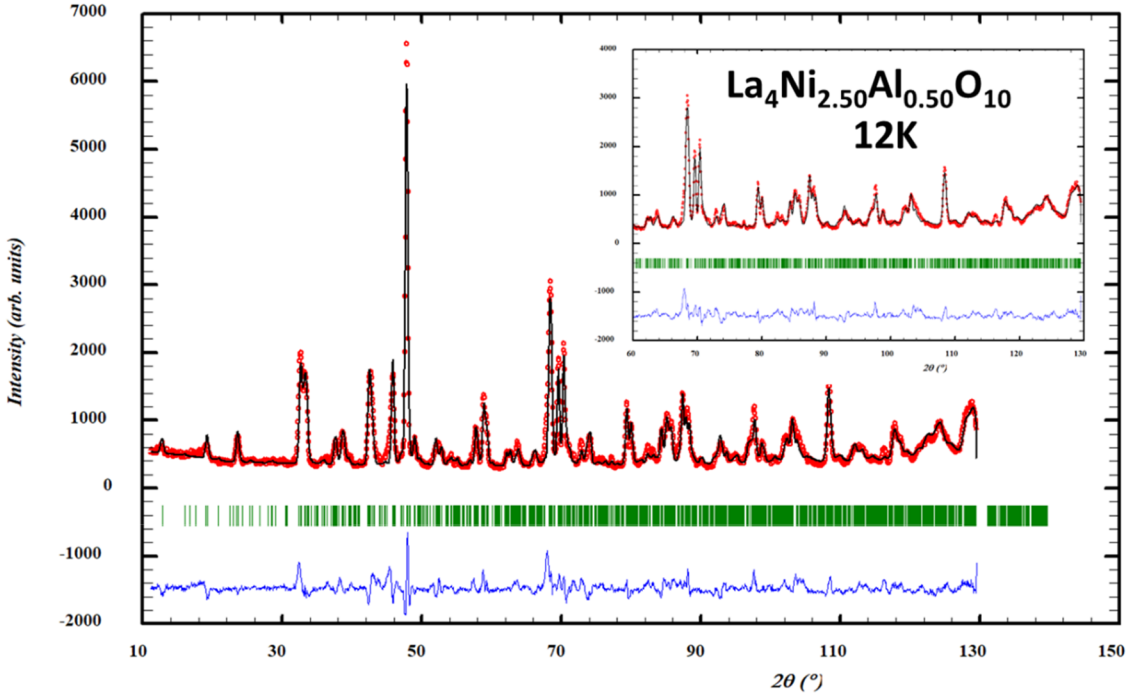

Figure 4. Observed, calculated, and difference intensity profile for Rietveld fit to powder neutron diffraction data of $La_4Ni_{2.50}Al_{0.50}O_{10}$, λ = 1.5558 Å. Space group *P*21/*a*.

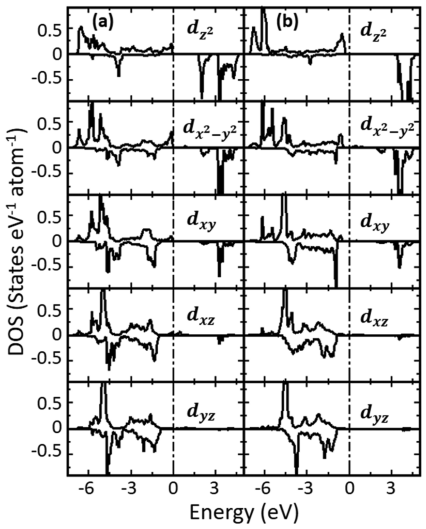

Figure 5. Orbital-projected DOS for Ni: (a) Ni1 and (b) Ni2 in ferromagnetic ground state for $La_4Ni_2AlO_{10}$ calculated by GGA + *U* with U_{eff} = 5 eV.

However, the extra contribution compared to the expected values of 0.5*e* for both ions (No oxidation state +2.5 on average) can be ascribed to hybridization between Ni 3d and O 2p. These results suggest that both Ni1 and Ni2 are in an intermediate average valence state between Ni^{2+} and Ni^{3+} and that no charge ordering is present. The average value of the diagonal components of the BECs tensor for $La_4Ni_2AlO_{10}$ is +2.4 and +2.7 for Ni1 and Ni2, respectively. The difference between the BECs of Ni1 and Ni2 of 0.3*e* is minor compared to a charge of 1*e*. Therefore, there is no indication for any Ni^{3+}−Ni^{2+} charge order with d^7 + d^8 species. The BEC for Al is ≈+2.9, close to its nominal ionic value of +3.

3.2. Magnetic Properties. Zero-field-cooled (ZFC) and field-cooled (FC) DC magnetization data (at 0.2 T persistent field) are shown for $La_4Ni_{3-x}Al_xO_{10}$ samples in Figure 6. For $La_4Ni_3O_{10}$, the ZFC and FC curves show two regimes; below 100 K, there is a weak tendency for localized paramagnetic behavior, whereas above 100 K, almost temperature-independent Pauli paramagnetic behavior exists. This is qualitatively in agreement with previous reports.[13,18] The $M(T)$ data for x = 0.02, 0.03, 0.05, and 0.15 (see Figure S3 in the Supporting Information) are qualitatively similar to those for $La_4Ni_3O_{10}$. We conclude that Pauli paramagnetic behavior prevails for $0 \leq x < 0.25$. A weak feature at around 60 K in some sets of FC data is ascribed to minute amounts of adsorbed oxygen, owing to a minute leakage in the PPMS and the high surface area of the wet chemically prepared oxide powders (∼1 μm particle size).

The magnetization $M(T)$ for x = 0.25, 0.75, and 1.00 is significantly higher than for Pauli paramagnetic samples at low Al contents (see Figure 6). Their temperature dependences are much more pronounced, suggesting localized paramagnetic moments. However, there are no well-behaved Curie−Weiss regions in the inverse magnetic susceptibility data (see insets in Figure 6). Nevertheless, a fit for the temperature range 150−300 K for x = 0.75 gives the parameters μ_{eff} = 3.51 μ_B and θ = −315 K, indicative of antiferromagnetic spin interactions (for x = 1.00; μ_{eff} = 3.31 μ_B; θ = −205 K). At temperatures below 20 K, a bifurcation develops in the ZFC and FC magnetization curves for the heavily Al substituted samples x = 0.75−1.00.

For x = 0.00, the $M(H)$ curve increases linearly with the applied field consistent with Pauli paramagnetic behavior (Figure 7a). For x = 0.25−1.00 (Figure 7b), a small hysteresis develops with increasing Al content. The magnetization at 4 K increases substantially with increasing Al content. However, no samples reach saturation at the maximum field of 9 T.

The introduced nonmagnetic (diamagnetic) Al^{3+} ions will themselves not contribute directly to the observed magnet-

https://doi.org/10.1021/acsaelm.1c00270
ACS Appl. Electron. Mater. 2021, 3, 2671−2684

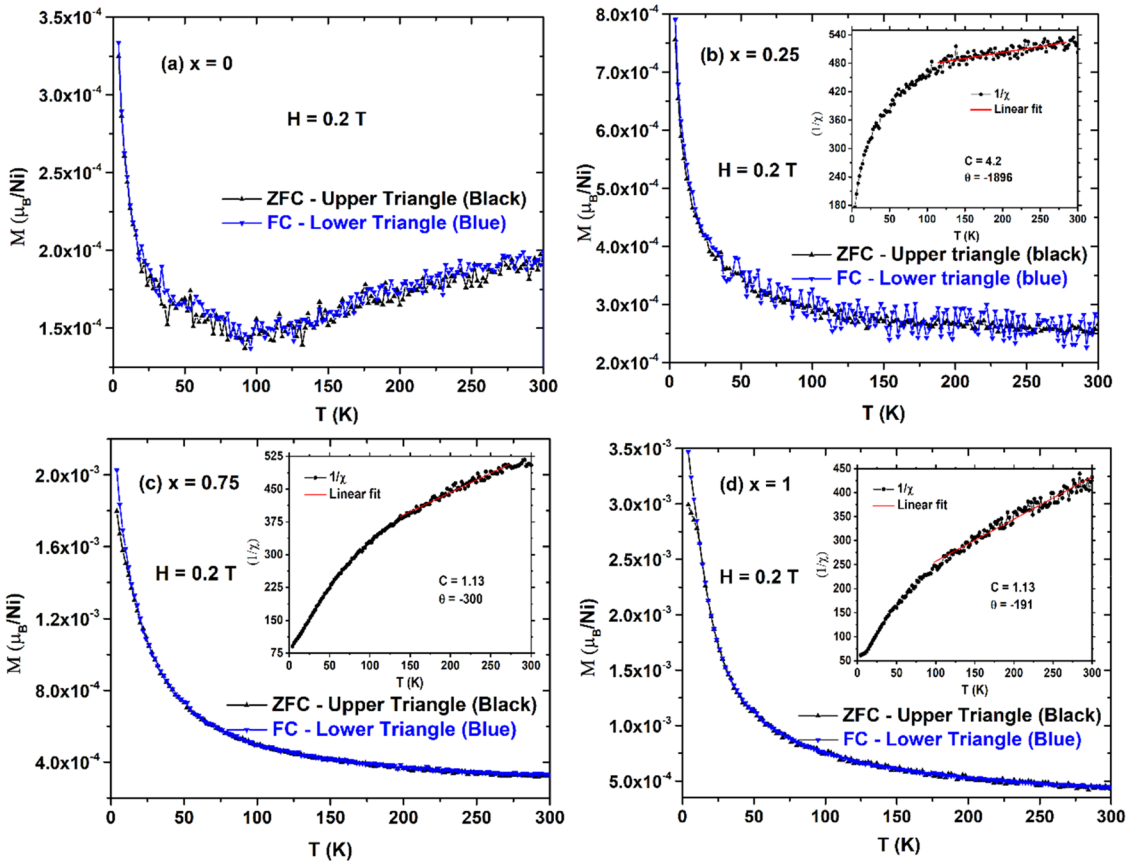

Figure 6. $M(T)$ magnetization data for $La_4Ni_{3-x}Al_xO_{10}$. Compositions (x) are given on the individual graphs (a–d). Data are measured in a field of 0.2 T. Insets show inverse susceptibility versus temperature.

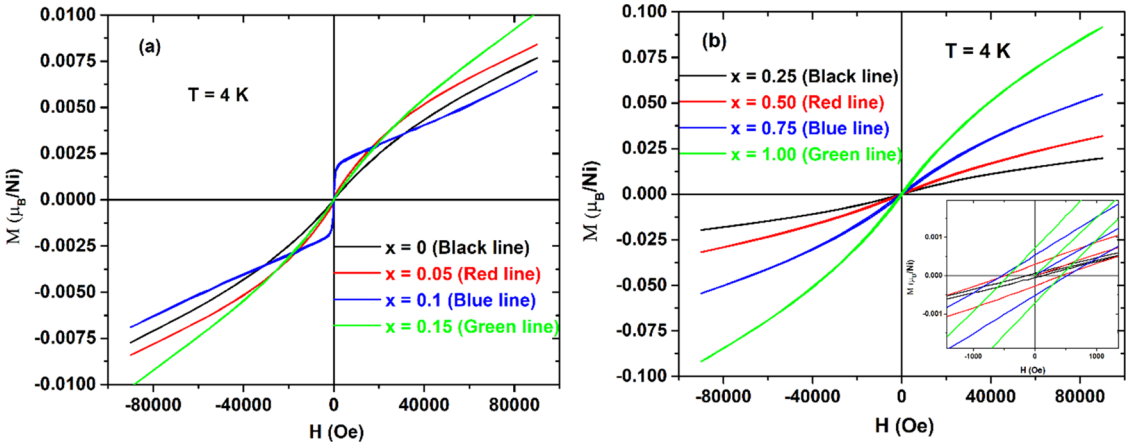

Figure 7. $M(H)$ data for $La_4Ni_{3-x}Al_xO_{10}$ at 4 K. Compositions (x) are given: (a) low Al contents and (b) higher Al contents. The inset in (b) highlights the hysteresis with increasing Al content.

ization. However, the substitution of Al^{3+} for $Ni^{2.67+}$ indirectly lowers the overall oxidation state of Ni from +2.67 [average valence of Ni sites (Ni^{2+} with $S = 1$ relative to $S = 1/2$ for Ni^{3+})] and hence a higher moment. An exchange mechanism is likely to exist between the Ni1 and Ni2 cations and mediated by O anions in the semiconducting/insulating regime of the solid solution (see below). Note that these exchange pathways between Ni1 and Ni2 (Ni1−O−Ni2) may partly be broken by nonmagnetic Al^{3+} cations, *i.e.*, by means of randomly inserted fragments of −Ni1−O−Al−O−Ni2−. Hence, we foresee the possibility of local islands with (weak) ferromagnetically interacting Ni cations in the material, whereas three-dimensional (3D) long-range ordering is prohibited. Interestingly, we note that ferromagnetic-like behavior is currently observed for $x = 0.10$ (see Figure 7a), with a small yet distinct jump in the magnetization close to zero applied external fields. We interpret the tiny hysteresis seen in Figure 7a to indicate small ferromagnetic-like islands in the material.

3.3. Resistivity—Electronic and Structural Transitions. The temperature dependence of the electrical resistivity (ρ) of $La_4Ni_{3-x}Al_xO_{10}$ is shown in Figure 8.

https://doi.org/10.1021/acsaelm.1c00270
ACS Appl. Electron. Mater. 2021, 3, 2671−2684

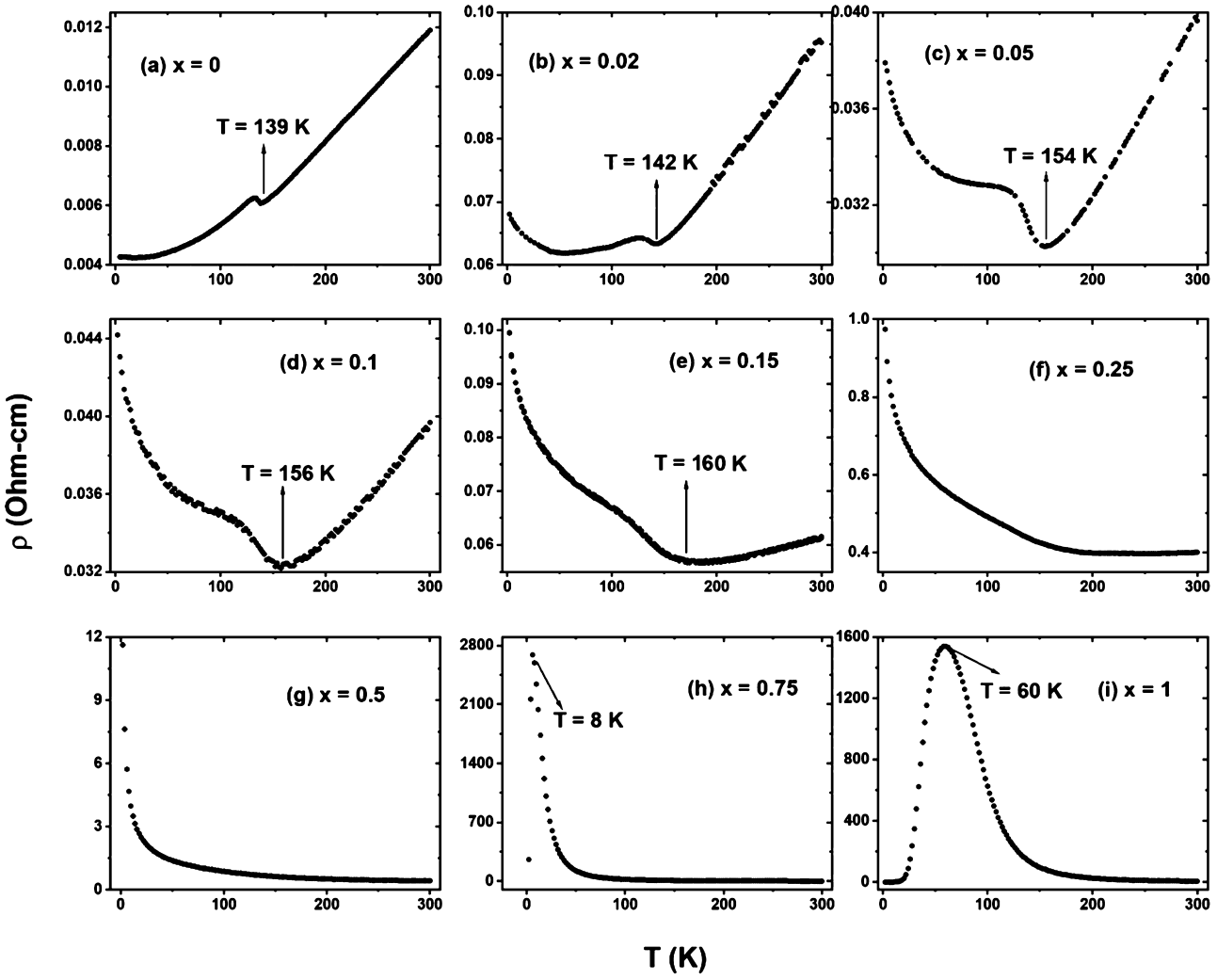

Figure 8. Resistivity versus temperature for $La_4Ni_{3-x}Al_xO_{10}$. Al substitution levels (x) are given on the individual graphs (a–i).

The resistivity curves for x = 0.00 and 0.02 in Figure 8a,b show two metallic regimes that are separated by a transition at around 140 K. For slightly higher Al contents, x = 0.05, the metallic range at low temperatures changes character toward nonmetallic (Figure 8c). With further increase of Al contents, the transition regime shifted to the high-temperature side and visible up to x = 0.15 (≈160 K) (Figure 8e). When the Al content is above the x = 0.15 level, the high-temperature metallic region vanishes, and for x = 0.25 and 0.50, semiconducting behavior is observed (Figure 8f,g). For x > 0.50, the samples become increasingly more resistive (Figure 8h,i). The observed variation in resistivity is quite extraordinary. We know that the two nonequivalent Ni1 and Ni2 atoms behave very similar with respect to bonding, ionicity, and charge state from diffraction and DFT analysis. Owing to our use of wet chemical synthesis routes and annealing efforts to ensure homogeneous Al distribution in the crystallites, these drastic changes are considered induced by Ni sublattice dilution and electron doping.

We recently reported in detail the physical properties of $La_4Ni_3O_{10}$ as a function of temperature and magnetic field.[18] Structurally, we then observed an anomaly in the unit cell parameters at the M-T-M (or the so-called CDW) transition around a temperature of 140 K. Through heat capacity measurements, we demonstrated that this transition was of second order, as also indicated by the variable-temperature diffraction data. A most striking aspect of the composition-dependent resistivity measurements in Figure 8 is the extent to which signatures related to the M-T-M/CDW transition can maintain themselves in the face of substitutional disorder until levels of x = 0.15. This broad compositional range where the transition is preserved and enhanced makes the Al substituted system the most exciting one to study for exploring the effects of doping and chemical pressure on the electronic properties of the 2D $La_4Ni_3O_{10}$. At higher Al contents, the M-T-M/CDW behavior is completely suppressed. We address two more important observations: (i) the temperature-dependent changes of the resistivity above and below the transition and (ii) the resistivity minimum with respect to the transition. For the high-temperature region (above the transition), we observe that the linear T dependence of metallic characters is maintained until x = 0.15, although the system gets relatively more resistive. The conduction regime changes to either higher-order or more complex power-law relations for x > 0.15. For x < 0.25, the samples are still within a metallic regime.

Fascinating changes take place in the low-temperature region (below the transition). We observe an immediate change for the resistivity minimum of $La_4Ni_3O_{10}$ at T = 20 K shifting to 50 K for x = 0.02 (Figure 8b). For $La_4Ni_3O_{10}$, this minimum is reported to be due to electron–electron scattering

https://doi.org/10.1021/acsaelm.1c00270
ACS Appl. Electron. Mater. 2021, 3, 2671–2684

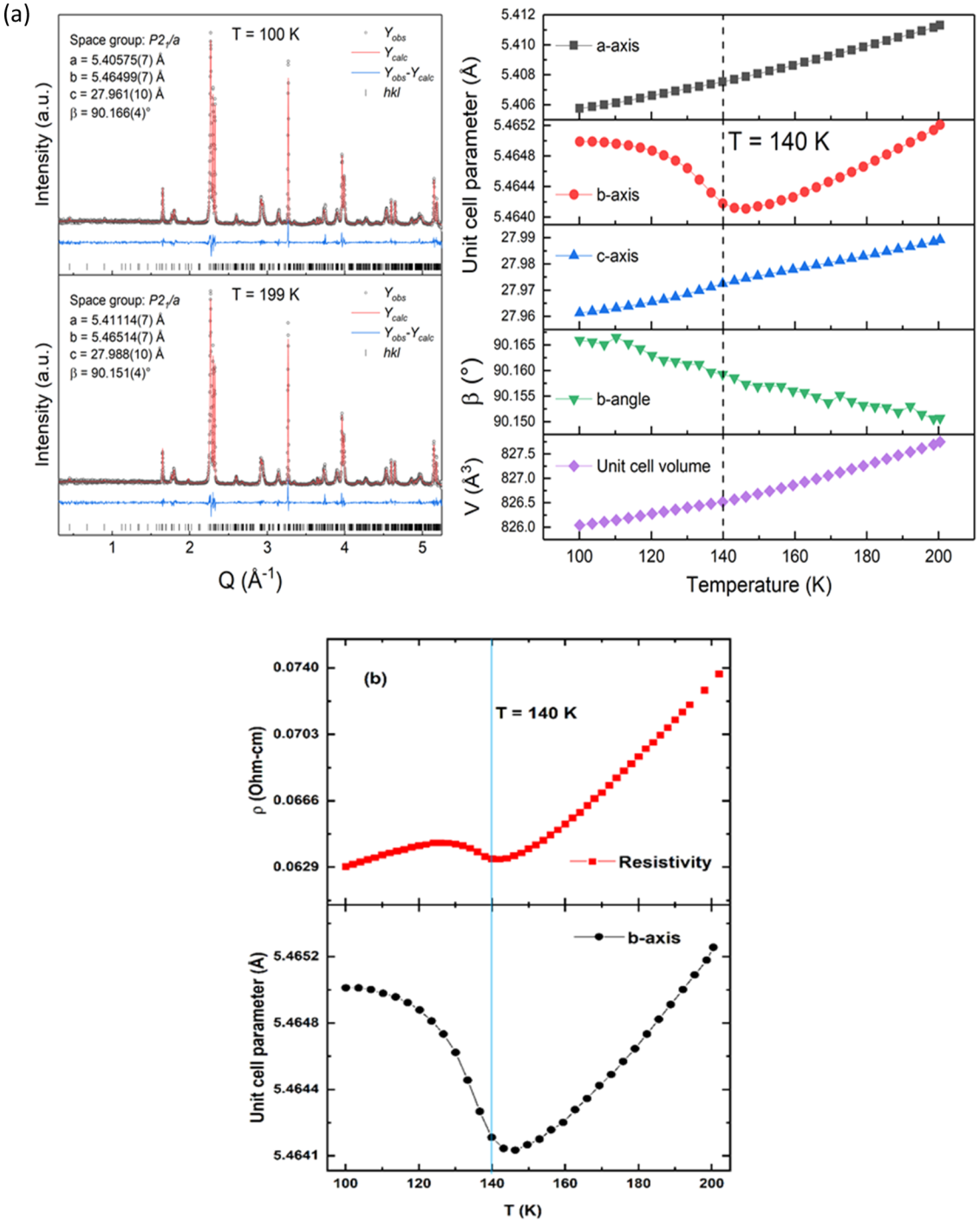

Figure 9. (a) Rietveld fit to high-resolution powder synchrotron diffraction data, space group $P21/a$ (left), and temperature dependence of unit cell dimensions for $x = 0.02$ (right). (b) Temperature dependence of unit cell dimension and resistivity data for $x = 0.02$ showing an excellent correlation of structural anomaly associated with the M-T-M transition.

events, generally showing $T^{-1/2}$ dependence. With gradual substitution of Al^{3+} into $La_4Ni_3O_{10}$ ($x \geq 0.02$), we observe a composition-dependent transformation from a M-T-M-like transition into an insulator-to-metal-like transition on increasing temperature (transition survives until $x = 0.15$) and the onset temperature becomes the new MIT and varies slightly with small changes in Al content, $T_{MIT} \approx 142$, 154, 156, and 160 K for $x = 0.02$, 0.05, 0.10, and 0.15, respectively. For $x = 0.05$, some 50−110 K below these onset temperatures, we observe a broad hump in resistivity. An exciting aspect is the fact that increased substitution of Al results in an enhancement of this hump and a noticeable upturn in resistivity, closely resembling what was reported for $Nd_4Ni_3O_{10}$ and $Pr_4Ni_3O_{10}$ (these have a compressed unit cell volume relative to $La_4Ni_3O_{10}$).[46,47] For $x = 0.25$ and 0.5, the samples are in the semiconductor regime. When Al content reaches the $x = 0.75$ level, where we see the hints of the first temperature-dependent MIT at the lowest temperatures (≈8 K) and this MIT moves to elevated temperatures ($T_{MIT} = 60$ K) for $x = 1.00$.

https://doi.org/10.1021/acsaelm.1c00270
ACS Appl. Electron. Mater. 2021, 3, 2671−2684

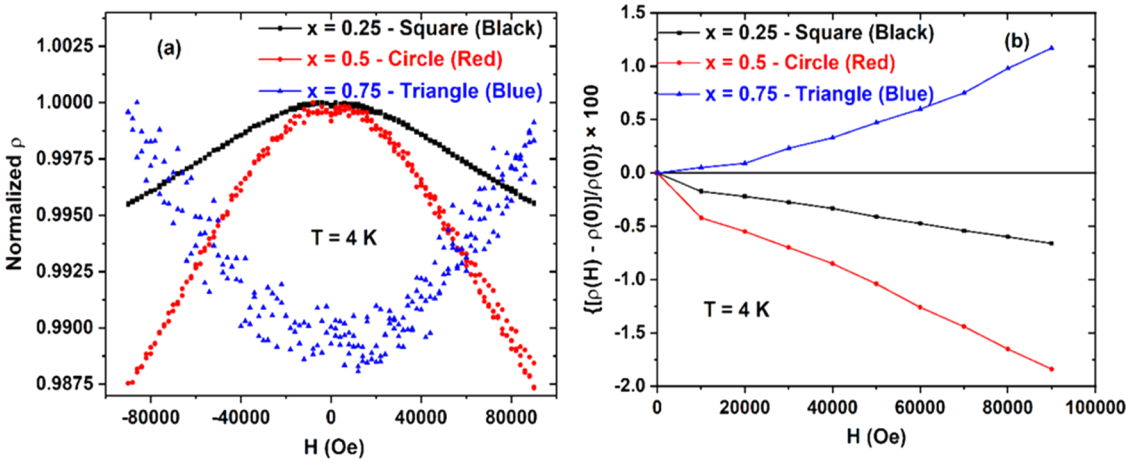

Figure 10. (a) Normalized resistivity for x = 0.25, 0.50, and 0.75 versus applied field at 4 K. (b) Variation in magnetoresistance for x = 0.25, 0.50, and 0.75 versus magnetic field.

For $La_4Ni_3O_{10}$, it has been speculated whether the metal-to-metal transition involves closely related distorted structures.[2,18] By means of high-resolution synchrotron powder diffraction, it was proved that the transition is connected with a structural anomaly, with $La_4Ni_3O_{10}$ being isostructural below and above the transition.[13,18] The current detailed analysis of variable-temperature synchrotron diffraction data for x = 0.02 shows a significant change in the b-axis (space group $P2_1/a$) at the M-T-M transition (Figure 9a). This structural transition correlates well with the anomaly in resistivity (Figure 9b). There is an excellent correlation between the resistivity and magnetization data shown by the metallic and Pauli paramagnetic regime for $La_4Ni_{3-x}Al_xO_{10}$ with $x < 0.25$ (Figures 6, S3, and S8).

At higher Al contents, a semiconducting/insulating state with localized moments occurs. A localization of electronic charge is probably occurring due to substitutional disorder and enhancement of anisotropy in conduction due to Al substitution. This results in increasing electron−electron scattering events as the Al content increases until a composition-dependent suppression of the M-T-M/CDW transition occurs. The introduction of Al^{3+} introduces disorder and more anisotropy, possibly weak Anderson localization, which quickly becomes evident in the low-temperature resistivity data. The substitution disrupts the conduction electron behavior, but without the resistivity jumping to high values. Since Al^{3+} is nonmagnetic, Pauli paramagnetic behavior will remain in the range where metallic conductivity is observed, up to $x < 0.25$. The 2D nature of the atomic arrangement of $La_4Ni_{3-x}Al_xO_{10}$ may possibly be mimicked by nickelate superlattices. These are foreseen to exhibit metal−insulator phenomena as outlined by Chaloupka and Khaliullin[48] and Park et al.[49] Recently, supporting literature toward such possible superlattice constructions is demonstrated for single crystals of $Pr_4Ni_3O_{10}$.[50] Interestingly, they reported that the in-plane ($\rho_\parallel$) resistivity below the M-T-M/CWD transition is enhanced by a factor of 6 at the lowest temperatures relative to the out-of-plane ($\rho_\perp$) resistivity, indicating extreme localization of charge carriers within the quasi-2D conduction layers.

3.4. Magnetoresistance. For $La_4Ni_{3-x}Al_xO_{10}$, we observe both positive and negative MR, dependent on the Al substitution level (Figure 10a). MR is shown for x = 0.25, 0.50, and 0.75 at 4 K in the field range $0 < H < 9$ T in Figure 10b; MR % = $\{[\rho(H) - \rho(0)]/\rho(0)\} \times 100$, where $\rho(H)$ and $\rho(0)$ are resistivities for the given applied magnetic field H and zero field, respectively.[51] As far as susceptibility data is concerned, we see a shift from low-substitution Pauli paramagnetic behavior transition into a localized paramagnet with possible short-range ferromagnetic ordering for x = 0.75 and 1.00.

Looking at it from the spin-dependent transport aspect, we observe a substitution-driven enhancement of the electronic nonuniformity (induces local magnetic moments), which increases spin-dependent scattering, resulting in a negative MR effect from x = 0.25 to 0.50, as seen previously in manganese perovskites.[52,53] Similar to the reported mechanisms for manganese perovskites, we observe an increase in disorder and anisotropy as more and more Al is substituted into $La_4Ni_3O_{10}$, and we note that both magnetic anisotropy and spin-polarized transport across grain boundaries (percolative transport) are sensitive to disorder and substitution and hence tend to affect MR and its sign directly.

For $0.25 \leq x \leq 0.50$, as the magnetic field increases, the (negative) MR increases in magnitude and reaches a maximum of −2% for x = 0.50. The light negative MR response is indicative here of a weak semiconductor with short-range antiferromagnetic interactions. However, at the value of x = 0.75 of Al substitution, there are fewer conduction pathways for those same majority spin carriers, and as a result, the MR effect is positive. The change in sign of the MR response indicates that the Al ions block increasingly more conduction pathways (Ni1−O−Al−O−Ni2) with short-range ferromagnetic interactions due to Al substitutional disorder and the samples become increasingly more resistive. Therefore, without the application of a magnetic field ($x > 0.50$), the spins of the prevailing ferromagnetic-like components (within nanometer-sized domains) are randomly oriented, and the transport is limited by spin scattering. Under an applied magnetic field, these small ferromagnetic-like islands are aligned, resulting in spin-dependent transport. The positive MR effect at higher Al^{3+} contents correlates with the increase in the ferromagnetic component, as seen in the $M(H)$ data at low temperatures, and furthermore, this correlates with the change in the average oxidization states of Ni upon Al^{3+} substitution.

https://doi.org/10.1021/acsaelm.1c00270
ACS Appl. Electron. Mater. 2021, 3, 2671−2684

3.5. Electronic Structure. The recent study on $La_4Ni_3O_{10}$ shows that the electronic structure is qualitatively similar for the monoclinic and orthorhombic variants.[2] Hence, we performed our studies in the higher-symmetric orthorhombic description since Al substitution involves expansion into large supercells. The electronic band structure of $La_4Ni_3O_{10}$ (*Bmab*) is shown in Figure 11a and exhibits features as reported in ref

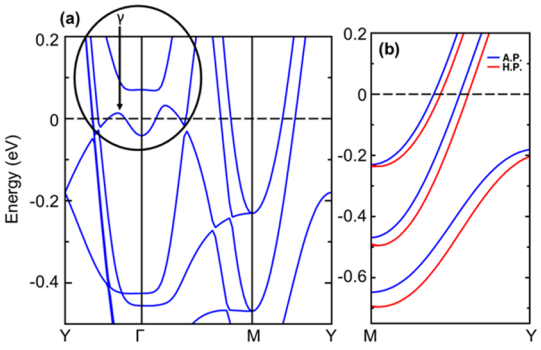

Figure 11. (a) Electronic band structure of $La_4Ni_3O_{10}$ in the *Bmab* space group. (b) Electronic band dispersion along M−Y for the ground state at ambient pressure (AP) and high pressure (HP) with a 5% smaller unit cell volume.

2. The γ bands with d_{z^2} orbital characters are flattened in the vicinity of the Fermi level. This agrees well with the pseudogap obtained in the symmetrized energy distribution curves obtained at 24 K.[23] To clarify pressure effects on the electronic structure of $La_4Ni_3O_{10}$ caused by internal chemical pressure, a high-pressure (HP) situation with 5% less unit cell volume is compared with the ambient pressure (AP) phase (ground-state volume structure). These data are also relevant for isostructural compounds, where the La cation is exchanged with smaller rare-earth cations, and thus comparisons with $Nd_4Ni_3O_{10}$ and $Pr_4Ni_3O_{10}$. Note that the introduction of Al^{3+} gives a volume contraction, though less than 1% (see Figure 1).

The band dispersions along the M−Y line are compared in Figure 11b. We note that the bands become more dispersed for the HP situation. The increased dispersion is because of the pressure on the system, which can broaden the bandwidth by enhancing the band overlap.

This leads to a decrease in resistivity with increased pressure, which is consistent with a reduction in resistivity of $La_4Ni_3O_{10}$ with increasing pressure. Hence, $La_4Ni_3O_{10}$ remains metallic under pressure with an increase in conductivity because of the increase in bandwidth (so the effective carrier mass) compared to the ambient pressure case. These results are consistent with the pressure versus resistivity data obtained by Wu et al.[54]

The calculated total DOS for $La_4Ni_{3-x}Al_xO_{10}$, x = 0.00, 0.25, 0.50, and 1.00, in the ground-state magnetic configuration is given in Figure 12. We show the highest occupied energy level in the valence band (VB), E_F, by the dotted line. In the case of x = 0.00, finite DOS values are present near E_F (for both *Bmab* and *P*21/*a*). Hence, $La_4Ni_3O_{10}$ exhibits metallic character, consistent with resistivity measurements. For x = 0.25, 0.50, and 1.00, electrons start to localize, as seen from the reduced number of states at E_F. For x = 0.25, a finite band gap of 0.28 eV opens between the top of the VB and the bottom of the conduction band (CB), *i.e.*, x = 0.25 shows semiconducting behavior, consistent with experiments. The band gap evolution with increasing Al content is given in Table 1.

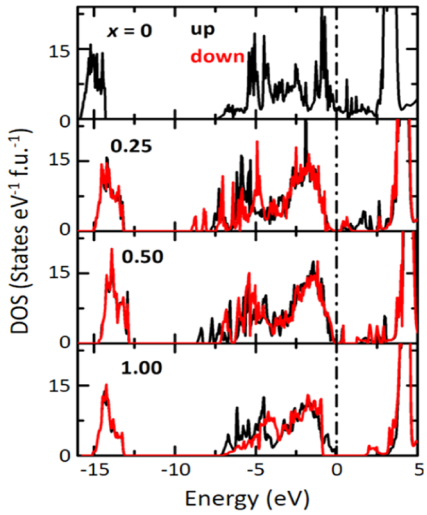

Figure 12. Total DOS for x = 0.00, 0.25, 0.50, and 1.00 calculated with GGA + U, U_{eff} = 6 eV. The black and red lines indicate the up and down spin channels, respectively.

Figure 13 shows the angular momentum-projected DOS for the La, Ni, and O atoms. The valence band of $La_4Ni_3O_{10}$ is primarily based on Ni 3d and O 2p admixtures. The negligibly small DOS contribution in VB from the La site indicates pronounced ionic bonding between La and O. The very similar topology of the DOS profile for the Ni sites supports the presence of an average valence state for all Ni atoms. The s and p states of Ni have a negligible contribution in VB in the vicinity of E_F. Furthermore, Figure 13 shows the partial DOS for the three types of oxygen atoms O1, O2, and O3 situated in the Ni1 layer, Ni2 layer, and La layer, respectively. The d states of Ni and p states of O are distributed over the range −7 eV to 4 eV. This implies that the Ni d and O 2p states are strongly hybridized, and the bands cross the Fermi level, resulting in metallicity. The O 2s states are localized around −14 eV. The inclusion of parameter U is necessary for stabilizing a ferrimagnetic ground state relative to a ferromagnetic state for x = 0.25, 0.50, and 1.

For U = 0, a metallic ferromagnetic state is favored. The results presented here refer to U = 6 eV and J = 1 eV. The calculated values for magnetic moments and the type of ground state ordering are given in Table 1. DFT calculations are consistent with Pauli paramagnetic ground state observed for $La_4Ni_3O_{10}$. For x = 0.25 and 0.50, a ferrimagnetic configuration is calculated as ground state, whereas x = 1.00 stabilizes in a ferromagnetic configuration. This is partly in agreement with experiments.

We do observe increased ferromagnetic interactions on increasing Al levels in M(T) and M(H) data; however, there is no indication for any long-range magnetic order. We note that the ferrimagnetic configuration is essential to model an appropriate semiconducting ground state for x = 0.25 and 0.50 that in turn will be consistent with the resistivity data. The calculated moment of some 1.4 μ_B (Table 1) is less than the 2S value derived from the Curie−Weiss fit; however, the latter region is not well defined in the $M(T)$ data (see Figure 6).

4. DISCUSSION

The metallic properties of $La_4Ni_3O_{10}$ are due to mixing of oxygen 2p and nickel 3d orbitals. For $La_4Ni_3O_{10}$, the e_g electrons and the average valency of Ni ions ($Ni^{+2.67}$) provide

https://doi.org/10.1021/acsaelm.1c00270
ACS Appl. Electron. Mater. 2021, 3, 2671−2684

Table 1. Calculated Ground-State Magnetic Ordering, Magnetic Moments of Ni Atoms, Ni−O Bond Length, Ni−O−Ni Bond Angle, and Band Gap for Al Contents of x = 0.00, 0.25, 0.50, and 1.00

Al content (x)	magnetic configuration	Ni1/Ni2 magnetic moment (μ_B)	average Ni1−O/Ni2−O bond length (Å)	Ni1−O−Ni2 bond angles in degree	band gap (eV)
0.00	paramagnetic		1.97/1.92	166.3	metal
0.25	ferrimagnetic	1.09/1.39	1.99/1.93	163.4	0.28
0.50	ferrimagnetic	1.36/1.50	2.02/1.94	162.3	1.12
1.00	ferromagnetic	1.43/1.72	2.04/1.96	161.4	1.81

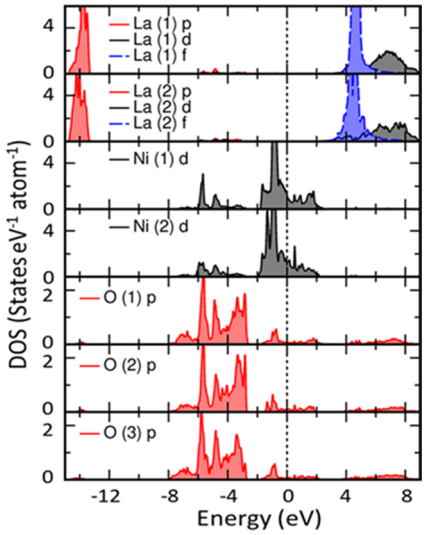

Figure 13. Angular momentum-projected DOS for the constituent atoms of $La_4Ni_3O_{10}$ calculated with GGA + U for U_{eff} = 6 eV.

the basis for electronic conductivity and magnetic exchange *via* O atoms. Homogeneous Al substitution in $La_4Ni_3O_{10}$ has at least three effects on the transport properties: first, by blocking pathways for electron jumping between Ni atoms located in the center of corner-shared NiO_6-octahedra; second, by reducing the overall oxidation state of nickel and thereby increasing Ni−O bond distances; and third, by opening up a gap at the Fermi level.

The Ni−O−Ni interactions are strongly perturbed by randomly distributed Al^{3+} cations in the structure. The absence of magnetic interactions connected to these Al^{3+} ions gives rise to Ni−O−Al−O−Ni structural fragments that weaken the magnetic exchange pathways and reduces the number of charge carriers that possibly participate in Ni1−O−Ni2 exchange interactions. Experiments show that the metallic behavior is completely lost at moderate levels of Al substitution. Hence, the Al-richer $La_4Ni_{3-x}Al_xO_{10}$ samples are semiconducting/insulating with electron hopping appearing as a likely conduction mechanism favoring double exchange. Meaning, a changeover from metallic to semiconducting to insulating behavior on Al substitution is seen. In terms of electronic structure, as described by DFT, the main effect of Al substitution is to lower the DOS at the Fermi level with the consequence that a band gap is opening, which increases in magnitude on increased Al substitution.

The electronic conductivity and the magnetic properties are extraordinarily dependent on the Al substitution level. With gradual substitution of Al^{3+} into $La_4Ni_3O_{10}$, we tend to align the low-temperature insulating phase to the nearest M-T-M/CDW transition, and the onset temperature becomes the new MIT until x < 0.25 (composition-dependent MIT). For x = 0.25−0.50, the material is in the paramagnetic semiconductor regime till the lowest of temperatures (as negative MR clearly supports at 4 K). Here, if there are any short-range ordering, it should be antiferromagnetic. When the Al content reached the x = 0.75 level, where there are hints of the first temperature-dependent MIT at the lowest temperatures (MR becomes positive) and this MIT moves to elevated temperatures at the x = 1.00 level (T_{MIT} = 60 K). At these compositions, the system is dominant (at low temperature) ferromagnetic-like ordering in the sea of a paramagnetic insulator.

The intriguing M-T-M transition of $La_4Ni_3O_{10}$ that attracts significant interests theoretically is retained at low Al levels (x = 0.15); however, at lower temperatures, the electric properties change even for lower x-values character toward a less conducting state. To explore these intriguing details at an ultralow substitution level, it is necessary to pay attention to material synthesis. Indeed, a wet chemical approach with gravimetrically analyzed precursors is a prerequisite for proper composition control as well for ensuring random Al distributions at the cationic sites and throughout all crystallites being in the submicrometer range. The present synchrotron diffraction data provide evidence of a minor yet significant change in some of the unit cell parameters at the M-T-M transition. Hence, there exists a distinct coupling, albeit probably being weak.

Both experiments and DFT indicate that the Ni cations take an average valence state (an intermediate, average oxidation number) with no indication for any Ni^{2+}—Ni^{3+} charge ordering (which possibly would have been appropriate for an ionic material). The surroundings for the two types of Ni atoms are different: the Ni atoms in the central part of the perovskite block are surrounded by six Ni atoms in neighboring octahedra, whereas the Ni atoms in the outer part of the perovskite block have just five such neighboring octahedra. Statistically, both Ni1 and Ni2 sites are in an average valence state intermediate between Ni^{2+} and Ni^{3+}, and one may envisage double exchange between the Ni cations by electron hopping to be operative and provide (weak) ferromagnetic interactions. The substitution of Al for Ni will cause an unavoidable break of such exchange Ni−O−Ni pathways, *i.e.*, through randomly inserted fragments of −Ni−O−Al−O−Ni−. Hence, local islands with (weak) ferromagnetic interactions may appear in the material. Similar behavior has previously been observed for alkaline-earth-substituted manganites like $La_{0.7}Ca_{0.3}MnO_3$.[55] We furthermore note a changeover from negative to positive magnetoresistance for x > 0.50. The enhanced (positive) MR effect at higher Al^{3+} contents correlates with an increase in the (short-range) ferromagnetic component seen in the $M(H)$ data at low temperatures, and furthermore with the lowered average oxidation of Ni caused by Al^{3+} substitution. The latter observation is interesting and points at a more general route to tune MR properties in $La_4Ni_3O_{10}$ and other Ruddlesden−Popper-type oxides, from a technological perspective.

https://doi.org/10.1021/acsaelm.1c00270
ACS Appl. Electron. Mater. 2021, 3, 2671−2684

5. CONCLUSIONS

In a metallic low-dimensional perovskite, such as $La_4Ni_3O_{10}$, electronic states are very sensitive to substitutional effects. The low-temperature phase is more often than not the first to show such fluctuations in transport behavior. As the system here already shows anisotropic conduction, to begin with, Al substitution would result in enhancement of both disorder and anisotropy possibly due to the preference of Al^{3+} substituent ion reducing conduction pathways −Ni−O−Al−O−Ni−. Indeed, we see such direct effects on electronic conduction pathways even at $x = 0.02$ substitution levels, where the low-temperature resistivity minima shift to elevated temperatures. With the introduction of slightly more Al^{3+}, $x = 0.05$, we observe the low-temperature state to completely transform into a semiconducting/insulating state. However, the high-temperature conduction, assisted mainly by phonons, sees minor changes only. What is striking is the intermediate-temperature region showing the transition (M-T-M/CDW), which enhances not only intensity, but also resistivity curve shape is strikingly similar to what is observed for $Nd/Pr_4Ni_3O_{10}$ counterparts,[46,47] indicating a contraction in the $La_4Ni_3O_{10}$ unit cell dimensions similar to the replacement of Nd/Pr for La. The underlying reason for the enhancement of the M-T-M/CDW transition for the moment remains unclear. Furthermore, we notice that the onset temperature of M-T-M/CDW becomes the new MIT temperature from $x = 0.02$ to $x < 0.25$, beyond which this transition is completely suppressed. However, at the same time, the low-temperature phase is truly semiconducting/insulating and is representative also in the MR, which is negative for $x = 0.25$, shows field-dependent reduction in spin transport of majority spin carriers, and is further lowered for $x = 0.50$. From $x = 0.02$ to 0.50, we observe a substitution-dependent MIT from a coexisting low-temperature paramagnetic insulating and high-temperature metallic state into a purely paramagnetic insulating state, which shows up in MR curve as a sharpening of the negative MR effect. For $x = 0.75$, we observe a temperature-dependent MIT at very low temperature and a sign change of MR from negative to positive with a ZFC-FC bifurcation, possibly indicating the creation of short-range ferromagnetic ordering of the ferromagnetic domains/clusters that are formed due to Al substitution (Ni1−O−Al−O−Ni2) in a paramagnetic insulating matrix. Finally, at $x = 1.00$, we observe the same ferromagnetic ordering strengthening as seen from magnetization curves taken at 4 K and an enhancement of the MIT temperature to around 60 K, possibly driven by polaron formation, as reported for manganese perovskites.[52,53,56] This subtle interplay of conduction properties with substitution and its influence on conduction pathways, where the substituent ions are nonmagnetic, makes $La_4Ni_{3-x}Al_xO_{10}$, a fascinating system to study in detail through transport, X-ray, and neutron (inelastic and total scattering) diffraction studies. The very recent studies of single crystals of RP3 nickelates shed important light on charge and spin density waves. Such studies should be extended to include Al substituted samples—if feasible for single-crystal growth.

■ ASSOCIATED CONTENT

Supporting Information

The Supporting Information is available free of charge at https://pubs.acs.org/doi/10.1021/acsaelm.1c00270.

$La_4Ni_{3-x}Al_xO_{10}$ composition details; crystal structure; powder XRD; and $M(T)$ magnetization data (PDF)

■ AUTHOR INFORMATION

Corresponding Authors

Manimuthu Periyasamy − *Centre for Materials Science and Nanotechnology, Department of Chemistry, University of Oslo, N-0315 Oslo, Norway;* Present Address: Quantum Nano Engineering Laboratory, Applied Physics Department, The Hebrew University of Jerusalem, Jerusalem 9190401, Israel.; orcid.org/0000-0001-5716-9083; Email: manimuthu.periyasamy@mail.huji.ac.il

Helmer Fjellvåg − *Centre for Materials Science and Nanotechnology, Department of Chemistry, University of Oslo, N-0315 Oslo, Norway;* orcid.org/0000-0001-6045-7211; Email: helmer.fjellvag@kjemi.uio.no

Authors

Lokanath Patra − *Department of Physics, Central University of Tamil Nadu, Nilakkudi, Tamil Nadu 610005, India;* Present Address: Department of Physics, Michigan Technological University, Houghton, Michigan 49931, United States.; orcid.org/0000-0002-1050-5665

Øystein S. Fjellvåg − *Department for Hydrogen Technology, Institute for Energy Technology, NO-2027 Kjeller, Norway;* orcid.org/0000-0003-0215-5260

Ponniah Ravindran − *Department of Physics, Central University of Tamil Nadu, Nilakkudi, Tamil Nadu 610005, India;* orcid.org/0000-0003-4611-011X

Magnus H. Sørby − *Department for Hydrogen Technology, Institute for Energy Technology, NO-2027 Kjeller, Norway*

Susmit Kumar − *Centre for Materials Science and Nanotechnology, Department of Chemistry, University of Oslo, N-0315 Oslo, Norway*

Anja O. Sjåstad − *Centre for Materials Science and Nanotechnology, Department of Chemistry, University of Oslo, N-0315 Oslo, Norway*

Complete contact information is available at: https://pubs.acs.org/10.1021/acsaelm.1c00270

Author Contributions

The manuscript was written through contributions of all authors. All authors have given approval to the final version of the manuscript.

Funding

The Research Council of Norway (RCN) project NOFCO (RCN 221905) as well as the Norway−India collaborative projects TESFUN and INNOREM (SIU 10089 and RCN 275014) are acknowledged for financial support.

Notes

The authors declare no competing financial interest.

■ ACKNOWLEDGMENTS

The authors thank Ingrid Marie Bergh Bakke for the synthesis of samples for powder neutron diffraction; SNBL@ESRF is gratefully acknowledged for providing beamtime at BM31 and excellent support; the Research Council of Norway project NOFCO as well as the Norway−India collaborative projects TESFUN and INNOREM are acknowledged for financial support.

REFERENCES

(1) Greenblatt, M. Ruddlesden−Popper $Ln_{n+1}Ni_nO_{3n+1}$ nickelates: structure and properties. *Curr. Opin. Solid State Mater. Sci.* **1997**, *2*, 174−183.

(2) Puggioni, D.; Rondinelli, J. M. Crystal structure stability and electronic properties of the layered nickelate $La_4Ni_3O_{10}$. *Phys. Rev. B* **2018**, *97*, No. 115116.

(3) Baiutti, F.; Gregori, G.; Suyolcu, Y. E.; Wang, Y.; Cristiani, G.; Sigle, W.; van Aken, P. A.; Logvenov, G.; Maier, J. High-temperature superconductivity at the lanthanum cuprate/lanthanum-strontium nickelate interface. *Nanoscale* **2018**, *10*, 8712−8720.

(4) Olafsen, A.; Fjellvåg, H.; Hauback, B. C. Crystal Structure and Properties of $Nd_4Co_3O_{10+\delta}$ and $Nd_4Ni_3O_{10-\delta}$. *J. Solid State Chem.* **2000**, *151*, 46−55.

(5) Ruddlesden, S. N.; Popper, P. The compound $Sr_3Ti_2O_7$ and its structure. *Acta Crystallogr.* **1958**, *11*, 54−55.

(6) Botana, A. S.; Pardo, V.; Norman, M. R. Electron doped layered nickelates: Spanning the phase diagram of the cuprates. *Phys. Rev. Mater.* **2017**, *1*, No. 021801.

(7) Zhong, R.; Winn, B. L.; Gu, G.; Reznik, D.; Tranquada, J. M. Evidence for a Nematic Phase in $La_{1.75}Sr_{0.25}NiO_4$. *Phys. Rev. Lett.* **2017**, *118*, No. 177601.

(8) Kajimoto, R.; Ishizaka, K.; Yoshizawa, H.; Tokura, Y. Spontaneous rearrangement of the checkerboard charge order to stripe order in $La_{1.5}Sr_{0.5}NiO_4$. *Phys. Rev. B* **2003**, *67*, No. 014511.

(9) Zhang, Z.; Greenblatt, M. Synthesis, structure, and properties of $Ln_4Ni_3O_{10-\delta}$ (Ln= La, Pr, and Nd). *J. Solid State Chem.* **1995**, *117*, 236−246.

(10) Anisimov, V. I.; Bukhvalov, D.; Rice, T. M. Electronic structure of possible nickelate analogs to the cuprates. *Phys. Rev. B* **1999**, *59*, No. 7901.

(11) Kajitani, T.; Hosoya, S.; Hirabayashi, M.; Fukuda, T.; Onozuka, T. Crystal structure of tetragonal form of La_2NiO_{4+x}. *J. Phys. Soc. Jpn.* **1989**, *58*, 3616−3623.

(12) Zhang, Z.; Greenblatt, M.; Goodenough, J. B. Synthesis, structure, and properties of the layered perovskite $La_3Ni_2O_{7-\delta}$. *J. Solid State Chem.* **1994**, *108*, 402−409.

(13) Nagell, M. U.; Kumar, S.; Sørby, M. H.; Fjellvåg, H.; Sjåstad, A. O. Structural and magnetic aspects of $La_4(Co_{1-x}Ni_x)_3O_{10+\delta}$ ($0 \le x \le 1$). *Phase Transitions* **2015**, *88*, 979−990.

(14) Jeon, S. Y.; Choi, M. B.; Hwang, J. H.; Wachsman, E. D.; Song, S. J. Oxygen excess non-stoichiometry and thermodynamic quantities of $La_2NiO_{4+\delta}$. *J. Solid State Electrochem.* **2012**, *16*, 785−793.

(15) Nagell, M. U.; Slawiński, W. A.; Vajeeston, P.; Fjellvåg, H.; Sjåstad, A. O. Temperature induced transitions in $La_4(Co_{1-x}Ni_x)_3O_{10+\delta}$; oxygen stoichiometry and mobility. *Solid State Ionics* **2017**, *305*, 7−15.

(16) Fjellvåg, H.; Hansteen, O. H.; Hauback, B. C.; Fischer, P. Structural deformation and non-stoichiometry of $La_4Co_3O_{10+\delta}$. *J. Mater. Chem.* **2000**, *10*, 749−754.

(17) Hansteen, O. H.; Fjellvåg, H. Synthesis, crystal structure, and magnetic properties of $La_4Co_3O_{10+\delta}$ ($0.00 \le \delta \le 0.30$). *J. Solid State Chem.* **1998**, *141*, 212−220.

(18) Kumar, S.; Fjellvåg, Ø.; Sjåstad, A. O.; Fjellvåg, H. Physical properties of Ruddlesden-Popper (n = 3) nickelate: $La_4Ni_3O_{10}$. *J. Magn. Magn. Mater.* **2020**, *496*, No. 165915.

(19) Tkalich, A. K.; Glazkov, V. P.; Somenkov, V. A.; Shilshtein, S. S.; Karkin, A. E.; Mirmelshtein, A. V. Synthesis, structure and properties of nickelates $R_4Ni_3O_{l0-\delta}$ (R = Nd, Pr, La). *Superconductivity* **1991**, *4*, 2280−2286.

(20) Ling, C. D.; Argyriou, D. N.; Wu, G.; Neumeier, J. Neutron diffraction study of $La_3Ni_2O_7$: Structural relationships among n = 1, 2, and 3 phases $La_{n+1}Ni_nO_{3n+1}$. *J. Solid State Chem.* **2000**, *152*, 517−525.

(21) Zhang, J.; Zheng, H.; Chen, Y. S.; Ren, Y.; Yonemura, M.; Huq, A.; Mitchell, J. F. High oxygen pressure floating zone growth and crystal structure of the layered nickelates $R_4Ni_3O_{10}$ (R = La, Pr). *Phys. Rev. Mater.* **2020**, *4*, No. 083402.

(22) Carvalho, M. D.; Cruz, M. M.; Wattiaux, A.; Bassat, J. M.; Costa, F. M. A.; Godinho, M. Influence of oxygen stoichiometry on the electronic properties of $La_4Ni_3O_{10\pm\delta}$. *J. Appl. Phys.* **2000**, *88*, 544−549.

(23) Li, H.; Zhou, X.; Nummy, T.; Zhang, J.; Pardo, V.; Pickett, W. E.; Mitchell, J. F.; Dessau, D. S. Fermiology and electron dynamics of trilayer nickelate $La_4Ni_3O_{10}$. *Nat. Commun.* **2017**, *8*, No. 704.

(24) Poltavets, V. V.; Lokshin, K. A.; Croft, M.; Mandal, T. K.; Egami, T.; Greenblatt, M. Crystal Structures of $Ln_4Ni_3O_8$ (Ln = La, Nd) Triple Layer T′-type Nickelates. *Inorg. Chem.* **2007**, *46*, 10887−10891.

(25) Patra, L.; Kishore, M. R. A.; Vidya, R.; Sjåstad, A. O.; Fjellvåg, H.; Ravindran, P. Electronic and Magnetic Structures of Hole Doped Trilayer $La_{4-x}Sr_xNi_3O_8$ from First-Principles Calculations. *Inorg. Chem.* **2016**, *55*, 11898−11907.

(26) Voronin, V. I.; Berger, I. F.; Cherepanov, V. A.; Gavrilova, L. Y.; Petrov, A. N.; Ancharov, A. I.; Tolochko, B. P.; Nikitenko, S. G. Neutron diffraction, synchrotron radiation and EXAFS spectroscopy study of crystal structure peculiarities of the lanthanum nickelates $La_{n+1}Ni_nO_y$ (n = 1, 2, 3). *Nucl. Instrum. Methods Phys. Res., Sect. A* **2001**, *470*, 202−209.

(27) Yashima, M.; Sirikanda, N.; Ishihara, T. Crystal Structure, Diffusion Path, and Oxygen Permeability of a Pr_2NiO_4-Based Mixed Conductor $(Pr_{0.9}La_{0.1})_2(Ni_{0.74}Cu_{0.21}Ga_{0.05})O_{4+\delta}$. *J. Am. Chem. Soc.* **2010**, *132*, 2385−2392.

(28) Jantsky, L.; Okamoto, H.; Thomas, M.; Karen, P.; Hauback, B. C.; Rosseinsky, M. J.; Fjellvag, H. Complex Magnetic Behavior in the $PrSr_3(Fe_{1-x}Co_x)_3O_{10-\delta}$ n = 3 Ruddlesden−Popper-Type Solid Solution with High Valent Cobalt and Iron. *Chem. Mater.* **2014**, *26*, 886−897.

(29) Minervini, L.; Grimes, R. W.; Kilner, J. A.; Sickafus, K. E. Oxygen migration in $La_2NiO_{4+\delta}$. *J. Mater. Chem.* **2000**, *10*, 2349−2354.

(30) Palgrave, R. G.; Borisov, P.; Dyer, M. S.; McMitchell, S. R. C.; Darling, G. R.; Claridge, J. B.; Batuk, M.; Tan, H.; Tian, H.; Verbeeck, J.; Hadermann, J.; Rosseinsky, M. J. Artificial Construction of the Layered Ruddlesden−Popper Manganite $La_2Sr_2Mn_3O_{10}$ by Reflection High Energy Electron Diffraction Monitored Pulsed Laser Deposition. *J. Am. Chem. Soc.* **2012**, *134*, 7700−7714.

(31) Battle, P. D.; Blundell, S. J.; Green, M. A.; Hayes, W.; Honold, M.; Klehe, A. K.; Laskey, N. S.; Millburn, J. E.; Murphy, L.; Rosseinsky, M. J.; Samarin, N. A.; Singleton, J.; Sluchanko, N. E.; Sullivan, S. P.; Vente, J. F. Colossal magnetoresistance in $Sr_{2-x}Nd_{1+x}Mn_2O_7$ (x = 0.0, 0.1). *J. Phys.: Condens. Matter* **1996**, *8*, L427−L434.

(32) Dwivedi, A.; Cormack, A. N. Crystal chemistry of Ruddlesden-Popper type structures in high Tc ceramic superconductors. *Bull. Mater. Sci.* **1991**, *14*, 575−584.

(33) Yaremchenko, A. A.; Kharton, V. V.; Bannikov, D. O.; Znosak, D. V.; Frade, J. R.; Cherepanov, V. A. Performance of perovskite-related oxide cathodes in contact with lanthanum silicate electrolyte. *Solid State Ionics* **2009**, *180*, 878−885.

(34) Carvalho, M. D.; Wattiaux, A.; Ferreira, L. P.; Bassat, J. M. Mössbauer investigation of ^{57}Fe doped $La_4Ni_3O_{10\pm y}$ phases. *J. Solid State Chem.* **2009**, *182*, 60−64.

(35) Demina, A. N.; Cherepanov, V. A.; Petrov, A. N.; Klokova, M. V. Phase Equilibria and Crystal Structures of Mixed Oxides in the La-Mn-Ni-O System. *Inorg. Mater.* **2005**, *41*, 736−742.

(36) Bruker AXS, *Topas v5: General Profile and Structure Analysis Software for Powder Diffraction Data*, Version 5; Bruker AXS: Karlsruhe, Germany, https://www.bruker.com/topas, 2013.

(37) Hauback, B. C.; Fjellvåg, H.; Steinsvoll, O.; Johansson, K.; Buset, O. T.; Jørgensen, J. The high-resolution Powder Neutron Diffractometer PUS at the JEEP II reactor at Kjeller in Norway. *J. Neutron Res.* **2000**, *8*, 215−232.

(38) Rietveld, H. M. Line profiles of neutron powder-diffraction peaks for structure refinement. *Acta Cryst.* **1967**, 22, 151; Rietveld, H. M. A profile refinement method for nuclear and magnetic structures. *J. Appl. Crystallogr.* **1969**, *2*, 65−71.

https://doi.org/10.1021/acsaelm.1c00270
ACS Appl. Electron. Mater. 2021, 3, 2671−2684

(39) Dyadkin, V.; Pattison, P.; Dmitriev, V.; Chernyshov, D. A new multipurpose diffractometer PILATUS@ SNBL. *J. Synchrotron Radiat.* **2016**, *23*, 825−829.
(40) Stephens, P. W. Phenomenological model of anisotropic peak broadening in powder diffraction. *J. Appl. Crystallogr.* **1999**, *32*, 281−289.
(41) Kresse, G.; Furthmüller, J. Efficient iterative schemes for ab initio total-energy calculations using a plane-wave basis set. *Phys. Rev. B* **1996**, *54*, 11169−11186.
(42) Monkhorst, H. J.; Pack, J. D. Special points for Brillouin-zone integrations. *Phys. Rev. B* **1976**, *13*, 5188−5192.
(43) Perdew, J. P.; Burke, K.; Ernzerhof, M. Generalized gradient approximation made simple. *Phys. Rev. Lett.* **1996**, *77*, 3865−3868.
(44) Schwarz, K.; Blaha, P.; Madsen, G. K. H. Electronic structure calculations of solids using the WIEN2k package for material sciences. *Comput. Phys. Commun.* **2002**, *147*, 71−76.
(45) Shannon, R. D. Revised effective ionic radii and systematic studies of interatomic distances in halides and chalcogenides. *Acta Crystallogr., Sect. A: Cryst. Phys., Diffr., Theor. Gen. Crystallogr.* **1976**, *32*, 751−767.
(46) Li, B. Z.; Wang, C.; Yang, P. T.; Sun, J. P.; Liu, Y. B.; Wu, J.; Ren, Z.; Cheng, J. G.; Zhang, G. M.; Cao, G. H. Metal-to-metal transition and heavy-electron state in $Nd_4Ni_3O_{10-\delta}$. *Phys. Rev. B* **2020**, *101*, No. 195142.
(47) Bassat, J. M.; Allancon, C.; Odier, P.; Loup, J. P.; Carvalho, M. D.; Wattiaux, A. Electronic properties of $Pr_4Ni_3O_{10\pm\delta}$. *Eur. J. Solid State Inorg. Chem.* **1998**, *35*, 173−188.
(48) Chaloupka, J.; Khaliullin, G. Orbital Order and Possible Superconductivity in $LaNiO_3/LaMO_3$ Superlattices. *Phys. Rev. Lett.* **2008**, *100*, No. 016404.
(49) Park, H.; Millis, A. J.; Marianetti, C. A. Site-selective Mott transition in rare-earth-element nickelates. *Phys. Rev. Lett.* **2012**, *109*, No. 156402.
(50) Huangfu, S.; Jakub, G. D.; Zhang, X.; Blacque, O.; Puphal, P.; Pomjakushina, E.; von Rohr, F. O.; Schilling, A. Anisotropic character of the metal-to-metal transition in $Pr_4Ni_3O_{10}$. *Phys. Rev. B* **2020**, *101*, No. 104104.
(51) Zhang, X. X.; Hernandez, J. M. Observation of colossal positive and negative magnetoresistance in perovskite-type manganese oxide $Nd_{0.67}Ca_{0.33}MnO_3$. *Europhys. Lett.* **1999**, *47*, 487−493.
(52) Alagoz, H. S.; Desomberg, J.; Taheri, M.; Razavi, F. S.; Chow, K. H.; Jung, J. Mechanism of sign crossover of the anisotropic magnetoresistance in $La_{0.7-x}Pr_xCa_{0.3}MnO_3$ thin films. *Appl. Phys. Lett.* **2015**, *106*, 082407−082411.
(53) Gavrichkov, V. A.; Ivanova, N. B.; Ovchinnikov, S. G.; Balaev, A. D.; Aminov, T. G.; Shabunina, G. G.; Chernov, V. K.; Petukhov, M. V. Comparison of negative magnetoresistance mechanisms in manganese perovskites and chromium spinels. *Phys. Solid State* **1999**, *41*, 1652−1655.
(54) Wu, G.; Neumeier, J. J.; Hundley, M. F. Magnetic susceptibility, heat capacity, and pressure dependence of the electrical resistivity of $La_3Ni_2O_7$ and $La_4Ni_3O_{10}$. *Phys. Rev. B* **2001**, *63*, No. 245120.
(55) Tiwari, S.; Phase, D. M.; Choudhary, R. J.; Mund, H. S.; Ahuja, B. L. Magnetic and electrical behavior of Al doped $La_{0.7}Ca_{0.3}MnO_3$ manganites. *J. Appl. Phys.* **2011**, *109*, 033911−033915.
(56) Periyasamy, M.; Fjellvåg, Ø. S.; Fjellvåg, H.; Sjåstad, A. O. Coupling of magnetoresistance switching and glassy magnetic state at the metal-insulator transition in Ruddlesden−Popper manganate $Ca_4Mn_3O_{10}$. *J. Magn. Magn. Mater.* **2020**, *511*, No. 166949.

https://doi.org/10.1021/acsaelm.1c00270
ACS Appl. Electron. Mater. 2021, 3, 2671−2684